

# A first glimpse at the Galactic plane with the ASKAP: the SCORPIO field

G. Umana<sup>1</sup>,<sup>1</sup>★ C. Trigilio,<sup>1</sup> A. Ingallinera<sup>1</sup>,<sup>1</sup> S. Riggi,<sup>1</sup> F. Cavallaro<sup>1,2</sup>,<sup>1,2</sup> J. Marvil,<sup>3</sup> R. P. Norris<sup>1</sup>,<sup>4,5</sup>  
A. M. Hopkins,<sup>6</sup> C. S. Buemi,<sup>1</sup> F. Bufano,<sup>1</sup> P. Leto<sup>1</sup>,<sup>1</sup> S. Loru,<sup>1</sup> C. Bordiu<sup>1</sup>,<sup>1</sup> J. D. Bunton,<sup>4</sup>  
J. D. Collier<sup>1</sup>,<sup>2,5</sup> M. Filipovic,<sup>5</sup> T. M. O. Franzen,<sup>7</sup> M. A. Thompson<sup>1</sup>,<sup>8</sup> H. Andernach<sup>1</sup>,<sup>9</sup> E. Carretti<sup>1</sup>,<sup>10</sup>  
S. Dai<sup>1</sup>,<sup>5</sup> A. Kapińska,<sup>3</sup> B. S. Koribalski<sup>1</sup>,<sup>4,5</sup> R. Kothes,<sup>11</sup> D. Leahy<sup>1</sup>,<sup>12</sup> D. McConnell,<sup>4</sup> N. Tothill<sup>5</sup>  
and M. J. Michałowski<sup>13</sup>

<sup>1</sup>INAF-Osservatorio Astrofisico di Catania, Via Santa Sofia 78, I-95123 Catania, Italy

<sup>2</sup>The Inter-University Institute for Data Intensive Astronomy (IDIA), Department of Astronomy, University of Cape Town, Private Bag X3, Rondebosch 7701, South Africa

<sup>3</sup>National Radio Astronomy Observatory, Domenici Science Operations Center 1003 Lopezville Rd, Socorro, NM 87801, USA

<sup>4</sup>CSIRO Astronomy & Space Science, P.O. Box 76, Epping, NSW 1710, Australia

<sup>5</sup>School of Science, Western Sydney University, Locked Bag 1797, Penrith, NSW 2751, Australia

<sup>6</sup>Australian Astronomical Optics, Macquarie University, 105 Delhi Rd, North Ryde, NSW 2113, Australia

<sup>7</sup>ASTRON: The Netherlands Institute for Radio Astronomy, PO Box 2, NL-7990 AA, Dwingeloo, the Netherlands

<sup>8</sup>Centre for Astrophysics Research, Department of Physics Astronomy & Mathematics, University of Hertfordshire, College Lane, Hatfield, Herts AL10 9AB, UK

<sup>9</sup>Departamento de Astronomía, DCNE, Universidad de Guanajuato, Callejón de Jalisco s/n, Guanajuato, Mexico

<sup>10</sup>INAF, Istituto di Radioastronomia, Via Gobetti 101, Bologna, Italy

<sup>11</sup>Dominion Radio Astrophysical Observatory, Herzberg Astronomy and Astrophysics, National Research Council Canada, PO Box 248, Penticton, BC V2A 6J9, Canada

<sup>12</sup>Department of Physics and Astronomy, University of Calgary, 2500 University Dr. NW, Calgary, AB T2N 1N4, Canada

<sup>13</sup>Astronomical Observatory Institute, Faculty of Physics Adam Mickiewicz University in Poznań, ul. Śloneczna 36, PL-60-286 Poznań, Poland

Accepted 2021 April 27. Received 2021 April 27; in original form 2021 January 19

## ABSTRACT

In the broad context of the Australian Square Kilometer Array Pathfinder (ASKAP) early-science phase and preparation for the related surveys, we report the first radio observations towards the Galactic plane. The targeted field was chosen to encompass the entire SCORPIO survey, one of the several pathfinder projects for the Evolutionary Map of the Universe survey planned with the ASKAP. The observations were carried out in 2018 January at a central frequency of 912 MHz, with 15 operational antennas, and covered a total area of about 40 square degrees in three different pointings. The final image has a resolution of  $24.1 \times 21.1$  arcsec<sup>2</sup> and a median rms of 541  $\mu$ Jy beam<sup>-1</sup>. We were able to extract 3545 candidate sources, 75 per cent of them point sources. For a preliminary validation, a comparison with the 843 MHz Molonglo Galactic Plane Survey is presented. Although the present observations were obtained with the ASKAP only partially deployed, its unique capability to map complex sources, such as those inhabiting the Galactic plane, at different angular scales, is highlighted. Within the SCORPIO field all the previously classified H II regions, Planetary Nebulae (PNe), and supernovae remnants (SNRs), previously known to be radio sources, were detected. We also report new radio detections from several H II regions previously classified as ‘candidates’ or ‘radio quiet’ and from half of all the PNe in the SCORPIO field with robust classification. Most notably, we find numerous unclassified, extended sources which constitute a promising sample of candidates H II regions and SNRs.

**Key words:** techniques: image processing – techniques: interferometric – surveys – stars: evolution – stars: formation – radio continuum: general.

## 1 INTRODUCTION

A new era in radio astronomy has finally arrived. The Square Kilometre Array (SKA) precursors have started their early-science phase with impressive results that foreshadow their full operation. In particular the Australian SKA Array Pathfinder (ASKAP, Hotan

et al. 2021) is transforming the way in which large radio surveys have been so far conducted. Due to the wide-field phased array feed (PAF) system (Chippendale, Hayman & Hay 2014) mounted on each antenna, ASKAP is capable of a huge instantaneous field of view,  $\sim 40$  square degrees, which allows the coverage of large areas of the sky in economical amounts of time (Leahy et al. 2019). The fully commissioned ASKAP has a survey speed of 220 deg<sup>2</sup> per hour at a target sensitivity of 100  $\mu$ Jy beam<sup>-1</sup> at 1.4 GHz, assuming

★ E-mail: [grazia.umanainaf.it](mailto:grazia.umanainaf.it)

a net bandwidth of 288 MHz and a resolution of 10 arcsec.<sup>1</sup> The ASKAP's early-science phase started in 2016 October using 12 of the 36 antennas present in the final design. As the commissioning operations have progressed, other antennas have been added and, at the time of the reported observations, 15 antennas were operational. A number of different regions of the sky were selected for testing the array in this phase: among these, one is centred towards the same field of the ‘Stellar Continuum Originating from Radio Physics in Our galaxy’ (SCORPIO) project (Umana et al. 2015; hereafter ‘Paper I’). We will refer to this targeted observation as to the ‘ASKAP SCORPIO observations’.

SCORPIO is a survey of an approximately  $2 \times 2$ -deg<sup>2</sup> area of sky centred at Galactic coordinates  $l = 343.5^\circ$ ,  $b = 0.75^\circ$ , conducted with the Australia Telescope Compact Array (ATCA) between 1.4 and 3.1 GHz (see Paper I for further details). Besides its own scientific goals, SCORPIO is used also as a technical test-bed for the Evolutionary Map of the Universe survey (EMU; Norris et al. 2011), an all-sky (Dec.  $< +30$  deg) ASKAP radio continuum sky survey scheduled to start in 2021, in particular helping to shape the strategy for its Galactic plane sections.

The Galactic plane has always been a formidable challenge for radio interferometers. A concentration of extended sources and the Galactic diffuse emission make it difficult to obtain a radio map devoid of imaging artefacts. This hampers the imaging performance of the instrument, reducing the quality of the final images (in terms of signal-to-noise ratio) and makes data reduction and analysis a particularly demanding task. Many of these issues have been mitigated by using different approaches and algorithms tuned for particular fields. However, because of the large quantity of data supplied by instruments such as the ASKAP, human intervention in every step of data reduction is infeasible and a general, though flexible, approach must be used.

In this work, we report the data reduction and analysis of the ASKAP observations of the SCORPIO field, conducted with the array still partially deployed. In Section 2, we describe the instrument set-up used and the data reduction pipeline. In Section 3, we focus on the point and extended source extraction, comparing our results to other similar surveys. Investigations of typical Galactic populations are also reported. A general discussion on the results and open problems is reported in Section 4. Finally, Section 5 summarizes this work and casts an outlook on future analysis and the ASKAP observations.

## 2 OBSERVATIONS AND DATA REDUCTION

### 2.1 The ASKAP observations

The SCORPIO field was observed with the ASKAP in band 1 (from 792 to 1032 MHz) in 2018 January using 15 antennas (of the 36 in the completed array) during the early-science phase. The array configuration had a minimum baseline of 22.4 m and a maximum baseline of 2.3 km. This implies that the observations, at the central frequency of 912 MHz, are sensitive to a minimum and maximum angular scale of 29.5 arcsec and 50 arcmin, respectively.

All the antennas were equipped with the version Mk II of the PAF specifically designed for ASKAP. Each PAF consists of 188 elements, 94 for each linear polarization. The data from each element are sent to the beamformer to create 36 independent beams, each one with a full width at half-maximum (FWHM) of 94.2 arcmin at 912 MHz. The

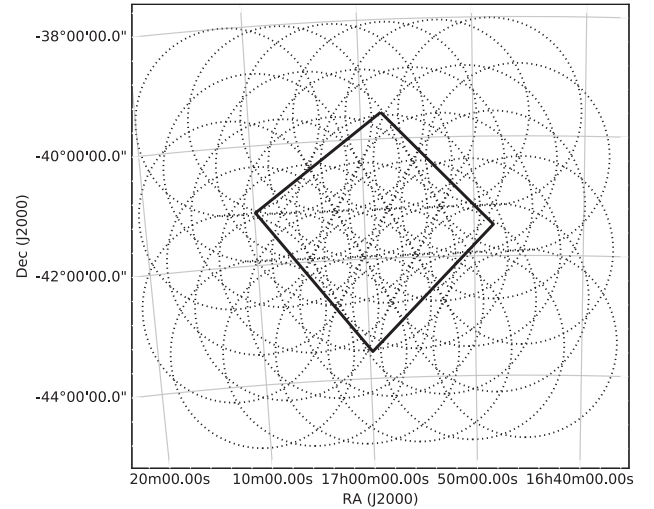


**Figure 1.** Comparison between the SCORPIO field coverage as observed by ATCA and by the ASKAP. The ATCA limits are represented as a solid thick line. For the ASKAP we report the position of the 36 beams (dotted circles) used for field A.

**Table 1.** Total observing time for each field including overheads for the bandpass and flux calibrator. The SB column reports the scheduling block ID for each data set. The observations of the field C are split in two different parts because of a hardware problem that occurred during observations.

Field	Source	SB	Time (h)
A	1934–638	5004	8
	SCORPIO	5008	
B	1934–638	5010	12
	SCORPIO	5011	
C	1934–638	5012	7
	SCORPIO	5013	
	1934–638	5014	4
	SCORPIO	5015	

total surveyed area covers  $\sim 40$  square degrees, which is larger by a factor 4.6 than the area covered in the previous ATCA observations (see Fig. 1). We refer to this as the ASKAP SCORPIO field in the rest of the paper.

The observations were carried out in the so-called ‘closepack36’ beam footprint (Hotan et al. 2021), consisting of three different pointings spaced by 51 arcmin with a 45-deg rotation, to optimize the sky coverage also at the highest frequency. The three pointings were conducted on three different days, and hereafter we refer to them as fields A, B, and C. The total integration time was 31 h including the observation of the standard bandpass and flux calibrator 1934–638 (see Table 1).

### 2.2 Data reduction

The data reduction process used the ASKAPSOFT package, based on CASACORE and specifically optimized for managing the ASKAP data (Whiting et al. 2019). The data reduction procedure is managed by a pipeline that configures and launches a series of jobs running on the Galaxy supercomputer at the Pawsey facility in Perth. As a first step data are copied from the storage location to the working area and a CASA measurement set is created for each of the 36

<sup>1</sup><https://www.atnf.csiro.au/projects/askap/config.html>

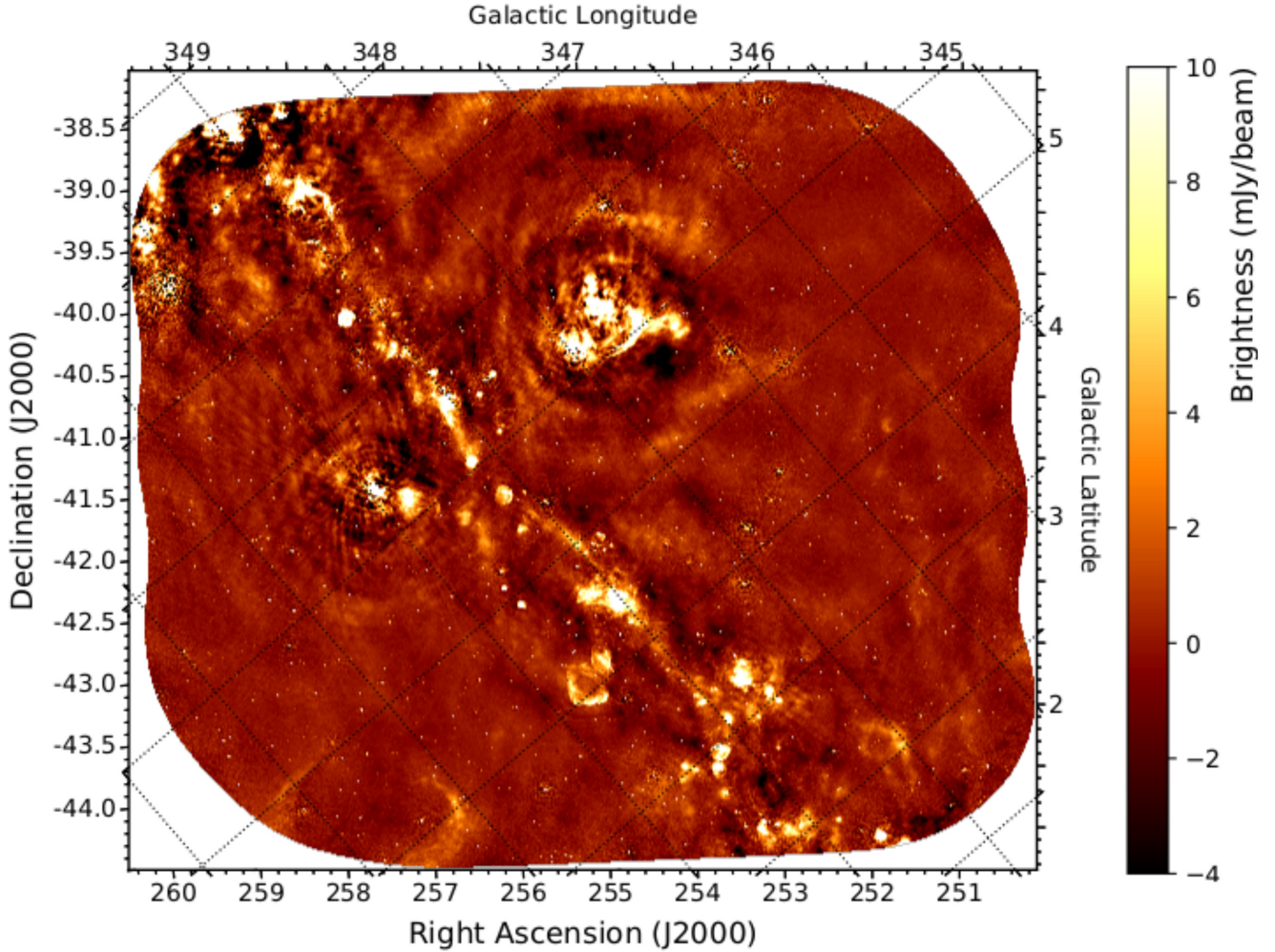


**Figure 2.** The ASKAP image of the SCORPIO field at 912 MHz. The mosaic covers a square region of  $\sim 40 \text{ deg}^2$ . The synthesized beam is  $24 \text{ arcsec} \times 21 \text{ arcsec}$  and the background rms noise is  $150\text{--}200 \mu\text{Jy beam}^{-1}$ , increasing to  $500\text{--}600 \mu\text{Jy beam}^{-1}$  close to the Galactic plane. The observations are sensitive to angular structures  $\lesssim 50 \text{ arcmin}$ . The silhouette of the Galactic equator is defined by a series of compact sources and bright H II regions. Several SNRs are also visible. Outside the Galactic plane some large and bright structures are evident. Among these, the region on the top centre of the field, at about  $2^\circ$  north from the Galactic plane, is the northern extreme of the Sco OB1 association, including the H II regions G345.45+1.50 and IC 4628. The other bright structure on the left, at about  $1^\circ$  south from the Galactic plane, is the H II region RCW 117.

beams. Automatic flagging is performed on bandpass calibrator and bandpass solutions are derived and applied to the target field. This, in turn, is subsequently flagged for bad data and averaged in the channel. A final flagging procedure is performed on the averaged data set. At this point, gain calibration solutions are derived. As a standard ASKAP procedure, no gain calibrator was observed during the observations (McConnell et al. 2016), because the PAF system requires an independent observation for each beam resulting in significant observing overheads. To proceed in the data reduction, a preliminary gain calibration is done using PKS 1934–638 as the calibrator, followed by several self-calibration iterations on automatically extracted bright sources present in the observed field. However this standard ASKAP reduction pipeline is best suited for extragalactic fields, where many of the brightest sources are point-like (e.g. Norris et al. 2006), and it can fail or behave in unpredictable ways for the Galactic plane where the radio sky is dominated by resolved sources and diffuse emission. To overcome this problem, we modified the standard procedure as follows. We restricted the self-calibration stage only to long baselines, selecting

data with  $\sqrt{u^2 + v^2} \gtrsim 3344\lambda$  (corresponding to a baseline of 1100 m at 912 MHz, or angular scale  $\lesssim 1 \text{ arcmin}$ ), a satisfactory value that we found, after attempting the data reduction with a variety of likely values. This step roughly filters out the extended emission while leaving point sources unaltered. The self-calibration is then performed and the solutions applied to all the other baselines. The self-calibration procedure is iterated three times, the first one, phase only, and then phase-amplitude self-calibration. The individual beams are finally imaged and combined together in a mosaic.

The three fields were processed separately with the final aim to merge all of them into a single map. However observations of fields B and C are affected by strong RFI and other correlator issues, as revealed from plots of the visibilities, and about 25 per cent of the data needed to be flagged.

The resulting images produced by the pipeline are therefore heavily corrupted. Manual flagging was performed on these fields to recover as much data as possible using the manual mode in the pipeline. The three fields were finally merged into a single image using a linear mosaicking procedure. The final map is shown in

Fig. 2. The synthesized beam is  $24 \times 21 \text{ arcsec}^2$  FWHM, while the background noise, calculated as the standard deviation of background pixel values, varies between  $\sim 130 \mu\text{Jy beam}^{-1}$  in regions far from the Galactic plane or other prominent extended sources and  $\sim 2 \text{ mJy beam}^{-1}$ , with a median value of  $541 \mu\text{Jy beam}^{-1}$ . The increase in background noise is mostly due to the imperfect cleaning of bright extended sources and the Galactic diffuse emission, which increases towards lower Galactic latitudes. With a maximum theoretical largest angular scale (LAS) of  $50 \text{ arcmin}$  at  $912 \text{ MHz}$ , radio structures with larger angular scales are therefore not adequately reconstructed and the image dynamic range is limited by imaging artefacts. To quantify the impact of artefacts, the residual sidelobe pattern around bright components has been measured in different regions of the ASKAP map. The obtained values vary within few per cent with position, but, in general, the artefacts due to a non-perfect cleaning determine a background noise of  $\sim 0.2$  per cent of the peak at a distance of  $10 \text{ arcmin}$  from the central source and, within this distance, the dynamic range is worse than 500.

### 3 SOURCE DETECTION

#### 3.1 Compact source extraction and preliminary validation

The last step of the ASKAPSOFT pipeline processing is an application of the source finder algorithm SELAVY (Whiting & Humphrey 2012) to create a compact source catalogue. Default SELAVY parameters includes the selection criteria considered in the FIRST survey (Becker, White & Helfand 1995). The source finder algorithm was run on the final mosaic combining the three available fields. 3140 source islands<sup>2</sup> were extracted from the map with peak flux density  $> 5\sigma$ , where  $\sigma$  is the local rms derived from the computed noise map. Each detected island is first processed to determine the number of blended components and finally fitted with a number of Gaussian components to estimate the integrated flux density. Among other Gaussian fitting results, SELAVY provides, for each fitted component, the peak and integrated flux densities, with their errors, the position angle, and the major and the minor FWHMs of the Gaussian component, indicating both the fit and its deconvolved value, given the image's restoring beam. After this procedure, 3545 source components are obtained for the entire field.

A continuum validation report<sup>3</sup> is automatically generated at the end of the pipeline processing, comparing the obtained source counts to existing measurements and models reported in the literature. The comparison is done extrapolating the ASKAP data to a frequency of  $1.4 \text{ GHz}$ , assuming a spectral index  $\alpha = -0.8$  ( $S \propto \nu^\alpha$ ). The result of this comparison is reported in Fig. 3. The red dots represent the differential source counts (normalized by  $S^{-2.5}$ ) obtained with the SCORPIO ASKAP data extrapolated to  $1.4 \text{ GHz}$ . The blue dots correspond to a compilation of source counts measurements at  $1.4 \text{ GHz}$  (taken from Norris et al. 2011) fitted by a sixth-degree polynomial (dashed line).

A closer look at the plot shows that most of the SCORPIO sources are located above the fitted curve. This is again reasonable and compatible with observations towards the Galactic plane where we do expect a source excess with respect to extragalactic fields (e.g. Cavallaro et al. 2018).

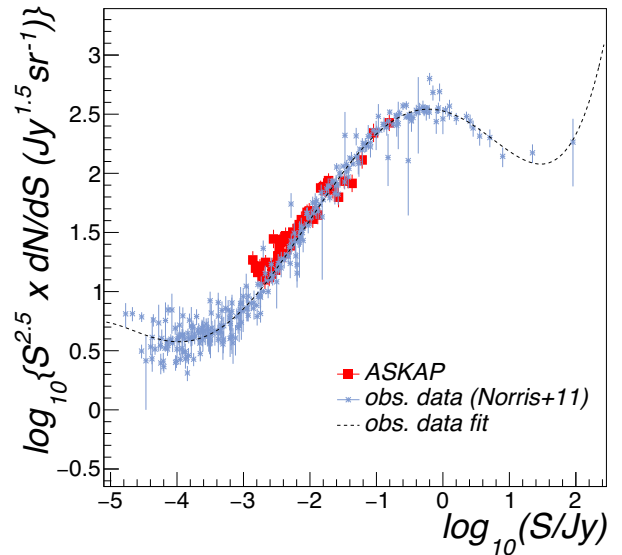


Figure 3. Differential source counts (red dots) observed with the ASKAP in

the Scorpio field, normalized by  $S^{-2.5}$ , as a function of the source flux density  $S$ . The ASKAP fluxes were extrapolated to  $1.4 \text{ GHz}$  (assuming an average spectral index  $\alpha = -0.8$ ) to be compared with data from Norris et al. (2011) (blue markers). The dashed line represents a sixth-degree polynomial fit of the experimental data collection.

In the companion paper (Riggi et al. 2021), the entire catalogue of the compact radio sources in the ASKAP SCORPIO field is presented. The typical performance achieved in source detection and characterization as well as the ASKAP positional and flux density scale accuracy are also discussed.

#### 3.2 Extended sources

To perform a first visual validation of the ASKAP map, we used the second epoch Molonglo Galactic Plane Survey (MGPS-2) survey (Murphy et al. 2007), conducted with the Molonglo Observatory Synthesis Telescope (MOST). We chose MGPS-2 because it covers the entire ASKAP SCORPIO field and it is conducted at a comparable frequency ( $843 \text{ MHz}$ ). However, the  $uv$ -plane coverage is considerably different. MOST is characterized by baselines ranging from  $15$  to  $1600 \text{ m}$ . As a consequence, the nominal resolution is around  $45 \text{ arcsec}$  and the maximum detectable LAS is approximately twice as large as that of the ASKAP.

For extended sources the comparison is therefore not straightforward, since differences in the angular scales probed by the two instruments heavily affect the reconstructed brightness and morphology of the source. Nevertheless, some interesting considerations can be made by examining a few sample sources.

In Fig. 4, the supernova remnant SNR G343.1–0.7 imaged with the ASKAP (panel c, right) is compared to the equivalent observation made with MOST (panel a, left). To validate the ASKAP image and to check for consistency, in the central panel, (panel b), of Fig. 4, the ASKAP image of SNR G343.1–0.7, convolved to the MOST beam, ( $\theta = 0.9 \text{ arcmin}$ ), is shown. While the overall structure of the remnant is well recovered by both instruments, the ASKAP image is sharper and more sensitive, revealing additional source structure and distinguishing unrelated background point sources that are not seen with MOST. We measured the integrated flux density of the source, in the ASKAP map, through aperture photometry, applying

<sup>2</sup>By ‘island’ we denote a group of connected pixels with fluxes above a merge threshold and around a seed pixel with flux above a detection threshold.

<sup>3</sup><https://confluence.csiro.au/display/askapsst/Continuum+validation+script>

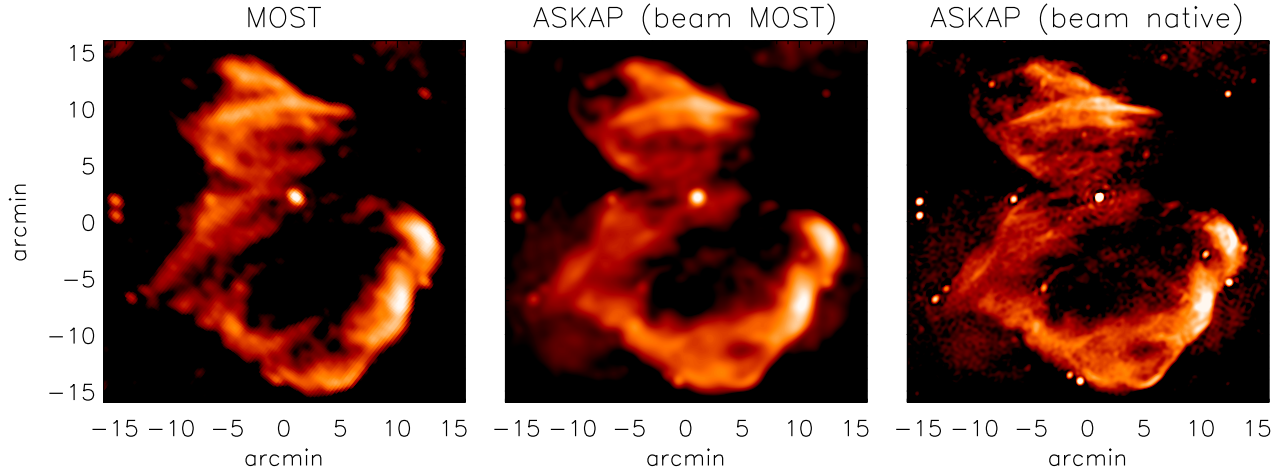


**Figure 4.** Images of SNR G343.1–0.7 as observed with MOST (left-hand panel) and with the ASKAP (right-hand panel). The ASKAP image of SNR G343.1–0.7, convolved to the MOST beam is shown in the central panel. The overall structure of the remnant is fully recovered by both instruments but finer details can be appreciated in the ASKAP map, where it is also possible to better distinguish sources unrelated to the remnant).

the background subtraction in a region surrounding the target, and obtained  $S_{\text{int}} = 7.46 \pm 0.01$  Jy, where the error associated with the integrated flux density is calculated according to  $\sigma_{\text{int}} = \text{RMS} \times (N_{\text{beams}})^{1/2}$ , where RMS is the noise of the map, measured outside the SNR and  $N_{\text{beams}}$  indicates the number of synthesized beams contained within the area we calculated the integrated flux density. If we, instead, measure the integrated flux density associated to the SNR but excluding the six point sources highlighted by the ASKAP (see Fig. 4, panel c), we obtain  $S_{\text{int}} = 7.26 \pm 0.01$  Jy. The difference in the integrated flux densities is small but significant and for other supernovae remnants (SNRs) could be more extreme. Moreover, an accurate identification of point sources that are not related to the observed SNR and whose nature is not recognized would allow a more precise analysis of the spatially resolved radio spectra to identify spectral index changes within the SNR, to be used to probe different populations of relativistic electrons that produce the observed radio emission (Egron et al. 2017). The ASKAP image shows additional details not visible in the previous MOST image. In particular, the brighter regions near the southern edges of the remnant have much greater spatial definition. These regions are potentially interacting with the local ISM and can be used to localize shocked regions.

Another illustrative example is reported in Fig. 5, where we compare the same field centred on the H II region [C06] S17 (Churchwell et al. 2006) as observed with MOST, ASKAP, and ATCA. The ATCA observations have already been presented and discussed in Paper I. Despite the great difference in terms of instrument capabilities, the overall morphology of the source is again well reconstructed by the ASKAP, which provides a good compromise between fine details and extended structures. All the compact components and detailed edges of the inner region, as detected in the ATCA image, are indeed present in the ASKAP map. Additionally, all the extended diffuse emission detected in the MOST map is also successfully recovered by the ASKAP, including the new detection of diffuse, low-brightness features in the southern part of the nebula. To compare the morphology of S17 at multiple wavelengths, we retrieved archival observations of the S17 region from Spitzer/GLIMPSE and Herschel/HiGAL. The diffuse emission recovered by the ASKAP appears to trace the ionized part of the

more extended material embracing the H II region, which is also rich in both warm and cooler dust as probed by mid-IR (Spitzer) and far-IR (Herschel) observations (Fig. 6). These examples indicate the superior capability of the ASKAP, compared to other radio facilities in the Southern hemisphere, to recover fainter extended features and, at the same time, to highlight small angular scale details.

### 3.3 Known Galactic sources

The radio component of the Galactic plane consists of diffuse emission as well as of the contributions of discrete radio sources. Major radio surveys (Condon & Kaplan 1998; Helfand et al. 2006; Wang et al. 2018) have indicated H II regions, PNe, and SNRs as the brightest and more numerous populations of Galactic radio objects. However, the census of each of these types of object is still incomplete and has been hampered by a combination of issues, related to the capabilities of existing radio surveys, including limited frequency range, sky coverage, sensitivity, resolution, and  $uv$ -plane coverage.

In particular, for PNe, estimates from theoretical counts indicate that there could be up to 46 000 PNe in our Galaxy but this number could be strongly reduced to ( $\sim 6600$ ) if it is assumed that only binary stars form a PN (Jacoby et al. 2010; Sabin et al. 2014). However, our census of PNe is largely off the expected number as the most up-to-date number of detected Galactic PNe is of only  $\sim 3600$  (Parker, Bojićić & Frew 2016). There are populations of PNe completely missed, probably those located very close to the Galactic plane, where the H  $\alpha$  emission, which indicates the presence of a thermal nebula, suffers from strong extinction (Ingallinera et al. 2016).

In the case of SNRs only 294 are known in our Galaxy (Green 2019), while models predict about 1000 (Tammann, Loeffler & Schroeder 1994). Existing surveys for SNRs are strongly biased towards bright and extended objects and the missing population is probably comprised of the youngest (most compact) and of lowest surface brightness SNRs.

A complete sample of PNe and SNRs will constrain their density and hence their formation rate and distribution in the Galaxy, with strong implications for models of both solar-type and massive stellar evolution.

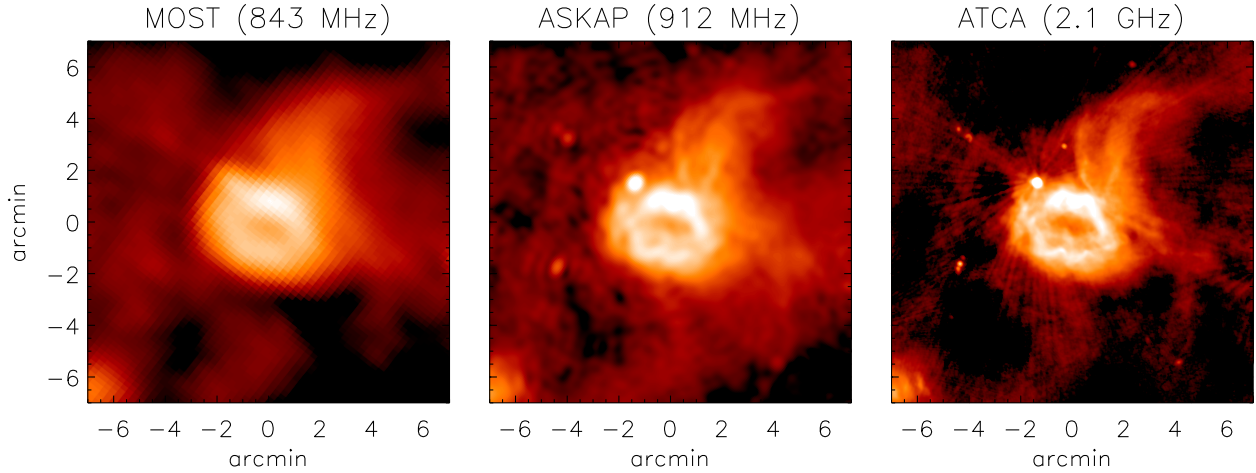


**Figure 5.** Images of the H II region [C06] S17 as observed with MOST, ASKAP, and ATCA.

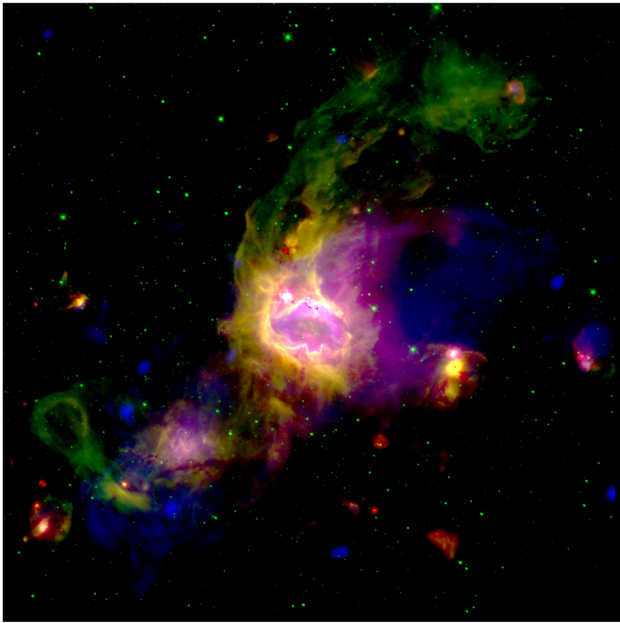


**Figure 6.** An RGB false colour image of the field around S17 in both dust and ionized gas. The colour-code is: green, from Spitzer/Glimpse (IRAC, 8  $\mu$ m); red, from Herschel/Hi-GAL (PACS, 70  $\mu$ m); and blue, from the ASKAP, 912 MHz. The image, 33 arcmin  $\times$  33 arcmin in size, is centred at  $l, b = 343.48^\circ, 0.026^\circ$ . The position of the S17 Bubble, as reported in Churchwell et al. (2006), is  $l, b = 343.482^\circ, -0.044^\circ$ .

In the following analysis, the detection of known radio H II regions, PNe, and SNRs by our ASKAP observation are assessed by visual inspection at positions provided by relevant catalogues.

As the purpose of this paper is a summary of the project focusing on the potentiality of the ASKAP in the field of Galactic radio astronomy, for each different category of Galactic sources considered in this section, we will exclusively provide the source identification and, if present in the compact catalogue provided by SELAVY, the integrated flux density. As indicated in session 3.1, a source is extracted by SELAVY if it satisfies the detection criterion (flux density  $\geq 5\sigma$ , where  $\sigma$  is the local rms), and if its spatial structure can

be accurately fitted by a small number of Gaussian components (Whiting & Humphrey 2012).

### 3.3.1 H II regions

H II regions are found in star-forming sites, in the vicinity of high-mass stars, where the gas is ionized by ultraviolet photons from the central object. They are tracers of the current epoch star formation and their continuum radio emission is due to thermal Bremsstrahlung radiation. The most complete catalogue of Galactic H II regions has been compiled by Anderson et al. (2014). To select H II regions, the authors used mid-infrared (MIR) observations from the Wide-Field Infrared Survey Explorer (WISE) satellite, taking advantage of the typical morphology that H II regions show in the MIR. The Anderson et al. (2014) catalogue has 8399 entries and consists of 1524 sources with robust classification as true H II regions, because they have measured RRL or  $H_\alpha$  emission. The others are classified as *candidates*, either with spatially coincident radio continuum emission (1986 sources) or without a radio counterpart (4124 sources). The latter are indicated in the catalogue as *radio quiet*. Among the possible *candidates*, there are 115 with no radio data available.

Within the ASKAP SCORPIO region, there are 382 sources, catalogued by Anderson et al. (2014) as follows: 97 known H II regions (K), 38 candidates (C), 220 radio quiet (Q), 22 closely located to a known H II regions (G), and five without radio data available. From a visual inspection of the ASKAP SCORPIO field we conclude that all 97 known (K), all 38 candidate (C) and all 22 grouped (G) H II regions were detected. Furthermore, 99/220 of radio-quiet sources (Q) and all of the five sources, which were previously reported without radio data available, were also detected in our ASKAP observations, bringing the total number of detections to 261. Fig. 7 shows a portion of the ASKAP SCORPIO field with the H II regions from Anderson et al. (2014) highlighted.

Ingallinera et al. (2019) present a catalogue of extended sources detected with ATCA in the SCORPIO sub-field. They extracted 99 extended sources, including nine H II regions reported by Anderson et al. (2014) as radio quiet and pointed out the presence of 18 H II regions, previously indicated as radio quiet, detected as point sources, without providing, however, their name or positions. Eight out of the nine extended sources, reported by Ingallinera et al. (2019), are also

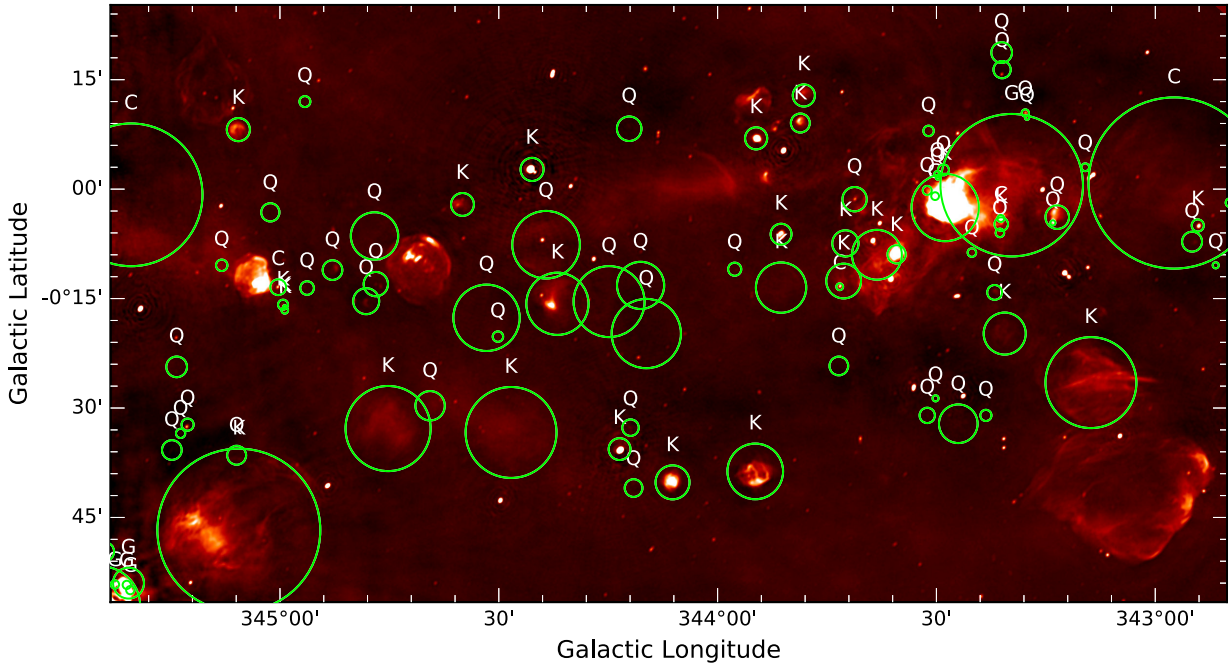


**Figure 7.** A portion of SCORPIO field centred at position  $l, b = 343.8^\circ, -0.2^\circ$ . The H II regions defined by Anderson et al. (2014) are indicated as ‘C’ candidates, ‘K’ known, ‘G’ group, ‘Q’ quiet.

present in our sample of sources detected by visual inspection of our ASKAP image, but we were not able to check if any other sources were in common. Our final sample of new detections consists of the 5/5 with no radio observations available plus the 91 previously reported as radio quiet, yielding a total of 96 new detections.

As anticipated in Section 3.3, we produce a catalogue for the 112 sources detected by visual inspection and extracted by SELAVY (Table 2). The catalogue reports the object WISE name as in Anderson et al. (2014), the coordinates (RA and Dec.), the classification following Anderson et al. (2014), the integrated flux density and its associated error, the angular dimensions of the source, FWHM of the major ( $\theta_{\max}^d$ ) and the minor ( $\theta_{\min}^d$ ) axes of the source, as determined by the Gaussian fit, deconvolved by the synthesized beam. Table 2 is truncated and its complete version is available in the online version of the paper.

In the ASKAP image we detect 45 per cent of the sources previously classified as radio quiet. Anderson et al. (2014) provide different hypotheses on the nature of these radio-quiet H II regions candidates. Among them, the possibility that these sources, characterized in the MIR by the same morphology as H II regions, could be instead intermediate-mass stars that do not have the necessary UV radiation to ionize the nebula surrounding the central object, or perhaps H II regions in the very early or very late stage of their evolution. These authors, however, provide a hint on the angular dimension of the infrared selected radio-quiet H II regions. When considering the angular size distribution for WISE catalogue of H II regions, all the known, candidates, and group samples share the same distribution while the radio-quiet sources are significantly smaller. Since there is a relation between the dimension of the infrared and of the radio nebula (Bihr et al. 2016), we should expect to see different angular size distributions for the known H II regions and radio-quiet sources detected in our ASKAP image. In Fig. 8, the flux density and the angular dimension distributions for known (K) and radio-quiet

(Q) H II regions, detected and extracted by SELAVY, are shown. The angular size plotted in Fig. 8 is defined as  $\theta = \sqrt{(\theta_{\max}^d)^2 + (\theta_{\min}^d)^2}$ .

In general, radio-quiet H II regions appear to be fainter and more compact than known (K) H II regions and this corroborates the hypothesis that previous non-detections were related to sensitivity limits of previous radio surveys. Similar result has been very recently obtained by Armentrout et al. (2021), who performed sensitive 3 cm JVLA observations targeting a sample of infrared-identified ‘radio-quiet’ H II regions in the range  $245^\circ \geq l \geq 90^\circ$ .

Since no information on distance of our detected sample of sources previously classified as radio quiet is available, we are not able to reach a conclusion on their physical dimension. These H II regions candidates are either close and compact, if they are in the early stage of their evolution or more distant if more evolved.

The detection of several sources previously classified as radio quiet indicates the high potential of ASKAP observations for Galactic studies as a significant number of radio-quiet H II regions candidates are possibly H II regions detected via their radio continuum near 1 GHz. The ASKAP performance will improve even further when the full 36 antenna array data will be used, allowing for more sensitivity and higher angular resolution. Further investigations, using a wider sample of candidate radio-quiet H II regions detected with the ASKAP in its final configuration, will allow us to further constrain the nature of these sources.

### 3.3.2 Planetary nebulae

Thermal radio continuum is also radiated by the ionized nebulae known as Planetary Nebulae (PNe). The PN is a short-lived (a few  $10^4$  yr) evolutionary phase of stars with mass between 0.8 and 8  $M_\odot$ . Objects in this phase are of high relevance in recycling matter in the universe. They are responsible for enriching galaxies with

**Table 2.** H II regions and H II regions candidates detected and extracted with SELAVY. This truncated table is intended to show its content. The complete table is available in the online version of the journal.

SourceID	Obj. name [ABB2014] WISE	RA	Dec.	C	S <sub>912</sub> (mJy)	err (mJy)	$\theta_{\max}^d$ (arcsec)	$\theta_{\min}^d$ (arcsec)
J252.386-44.4413	G340.910+00.167	16:49:32.5	-44:26:28	K	407.62	4.17	170.6	165.6
J252.609-44.2916	G341.121+00.141	16:50:26.1	-44:17:29	Q	5.73	0.09	39.4	25.1
J253.083-44.4688	G341.207-00.232	16:52:20.0	-44:28:07	K	710.53	17.04	51.7	42.6
J252.505-44.0838	G341.238+00.335	16:50:01.1	-44:05:01	K	9.62	0.11	30.9	19.8
J253.177-44.4449	G341.271-00.265	16:52:42.4	-44:26:41	Q	35.74	0.25	29.1	20.9
J252.734-44.1584	G341.286+00.159	16:50:56.2	-44:09:30	Q	2.13	0.02	18.1	0
J252.726-44.1177	G341.314+00.190	16:50:54.3	-44:07:03	Q	20.84	0.11	12.6	4.8
J253.277-44.3868	G341.358-00.287	16:53:06.5	-44:23:12	K	82.14	1.29	76.5	65.6
J252.806-44.1087	G341.364+00.147	16:51:13.4	-44:06:31	Q	4.96	0.24	54.5	13.8
J252.637-43.9016	G341.438+00.383	16:50:32.8	-43:54:05	C	2.55	0.05	27.5	11.4
—	—	—	—	—	—	—	—	—

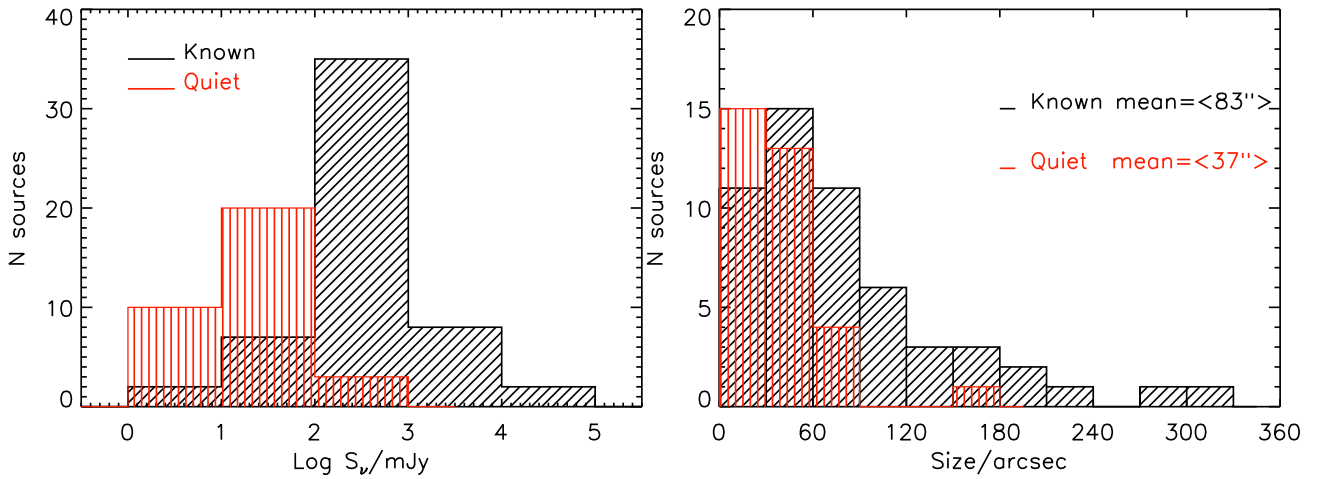


**Figure 8.** Flux density distribution (left-hand panel) and angular size distribution (right-hand panel) of H II regions, known, and radio quiet, detected with the ASKAP and extracted with SELAVY (see Table 2).

elements produced by stellar nucleosynthesis and thus trace the Galactic chemical enrichment process (Kwok 2007).

Parker et al. (2016) have compiled the most recent catalogue of Galactic Planetary Nebulae (HASH: Hong Kong/ AAO/ Strasbourg/ H $\alpha$ ). This catalogue is a unique data repository with a graphical interface, and currently contains multiwavelength images, spectra, positions, sizes, and morphologies of 3540 objects. For the following analysis we used the version as of 2016. These objects are classified as 2401 true (T) Galactic PNe, based on their multiwavelength PN-type morphologies and spectral features, 447 likely (L) Galactic PNe, based on the same parameters as for true PNe but with not completely conclusive imagery or spectroscopy, and 692 probable (P) Galactic PNe, where the available spectroscopy and/or imagery is not conclusive because of very low S/N spectra or a very low surface brightness of the nebula.

Within the ASKAP SCORPIO region, there are 48 sources catalogued by Parker et al. (2016), comprising 35 T, 6 L, and 7 P Galactic PNe. In the ASKAP map we detect 29/35 true PNe, 3/6 likely PNe, and 2/7 probable PNe, for a total of 34 radio sources.

In the case of true PNe, only 14 out of the 29 detected in the ASKAP maps have been already detected in the radio (Parker et al. 2016). We have therefore doubled the radio detections for these robustly classified Galactic PNe. We have further inspected the field of the non-detected true PNe. Four out of six of them are located in

a region with strong confusion, while the fifth is located in a region with a local rms of about 200  $\mu$ Jy. The last one is very weak and barely distinguishable from the noise.

It is also worthwhile to underline our new detections of three likely and two probable Galactic PNe that, considering the 15 new detections among our sample of true PNe, brings the total number of new detections to 20.

All the results are summarized in Table 3, where the object name, in bold if it is a new detection, the coordinates (RA and Dec.), the Galactic coordinates, the classification as in Parker et al. (2016), the integrated flux and its associated error, as determined with SELAVY, are reported. Four sources, detected by visual inspection, were not extracted by SELAVY. This failure of the source finder algorithm is probably related to a highly noisy background around these sources or to the fact that these sources do not fulfil all the imposed criteria. Fig. 9 shows these sources, while all the (other) new detections are shown in Fig. 10.

### 3.3.3 Supernova remnants

Other major polluters of the Galaxy are SNRs, the remains following the explosion of their progenitor stars. By enriching the interstellar medium (ISM) in heavy elements and other nucleosynthesis products, these stellar ejecta contribute to the chemical composition of

**Table 3.** PNe detected in the ASKAP SCORPIO field. New detections are highlighted in bold. Sources for which no flux density is reported are only detected by visual inspection. Column C indicates the classification following Parker et al. (2016).

Obj. name	RA	Dec.	l	b	C	S <sub>912</sub> (mJy)	err (mJy)
<b>PHR J1642–4212</b>	16:42:18.6	−42:14:45.20	341.723	+2.597	T	6.91	0.05
PN SuWt 3	16:44:24.1	−40:03:20.4	343.639	+3.733	T	3.68	0.04
Vd 1-3	16:49:32.9	−39:21:08.96	344.818	+3.432	T	2.48	0.04
<b>MPA J1650–4030</b>	16:50:20.2	−40:30:03.17	344.030	+2.582	T	5.5	0.05
Vd 1-4	16:50:25.3	−39:08:18.89	345.091	+3.439	T	3.23	0.03
Vd 1-5	16:51:33.7	−40:02:55.64	344.528	+2.690	T	4.99	0.06
PN H 1-3	16:53:31.3	−42:39:22.39	342.744	+0.752	T	35.18	0.14
<b>PHR J1653–4143</b>	16:53:55.3	−41:43:59.81	343.507	+1.277	T	14.59	0.07
Vd 1-6	16:54:27.3	−38:44:10.39	345.900	+3.086	T	14.35	0.13
<b>MPA J1654–4041</b>	16:54:43.2	−40:41:46.64	344.407	+1.814	L	9.53	0.06
<b>PN G343.6+01.1</b>	16:54:51.0	−41:43:49.91	343.618	+1.145	P	7.18	0.18
<b>IRAS 16515–4050</b>	16:55:00.4	−40:55:34.64	344.262	+1.627	T	8.72	0.03
<b>PN G345.8+02.7</b>	16:55:51.9	−39:00:20.95	345.862	+2.704	T		
PM 1-119	16:56:34.0	−43:46:14.77	342.226	−0.380	T	107.05	0.36
<b>MPA J1656–3912</b>	16:56:40.1	−39:12:36.83	345.800	+2.454	T	3.75	0.03
PN H 1-5	16:57:23.7	−41:37:57.86	343.992	+0.835	T		
IC 4637	17:05:10.5	−40:53:08.45	345.479	+0.140	T	233.11	0.62
<b>Vd 1-9</b>	17:05:38.9	−43:56:20.36	343.100	−1.775	T	9.54	0.10
PN Pe 1-8	17:06:22.6	−44:13:09.95	342.955	−2.049	T	83.62	0.39
<b>Kn 98</b>	17:06:19.6	−43:15:33.00	343.716	−1.463	L	7.19	0.07
<b>MPA J1706–4434</b>	17:06:49.3	−44:34:34.64	342.717	−2.327	T	8.32	0.07
PN H 1-6	17:06:59.1	−42:41:09.13	344.247	−1.215	T	34.85	0.12
<b>Wray 16 251</b>	17:07:30.6	−44:22:50.27	342.948	−2.308	T	37.89	0.29
<b>PN G343.9–01.6</b>	17:07:57.0	−43:09:04.93	343.980	−1.635	T	6.22	0.09
<b>PHR J1709–3931</b>	17:09:10.1	−39:31:06.50	347.030	+0.352	T		
PN H 1-7	17:10:27.4	−41:52:49.40	345.277	−1.249	T	180.98	0.75
<b>RPZM 3</b>	17:11:25.2	−39:29:51.68	347.305	+0.015	P	30.43	0.41
PM 1-131	17:12:22.0	−42:30:41.26	344.976	−1.907	T	3.61	0.02
<b>MPA J1713–4015</b>	17:13:10.8	−40:15:56.09	346.883	−0.710	T	9.55	0.08
<b>Kn 102</b>	17:14:25.0	−41:44:34.00	345.822	−1.765	L		
<b>PHR J1714–4006</b>	17:14:49.3	−40:06:08.96	347.199	−0.869	T	11.52	0.07
<b>MPA J1715–4303</b>	17:15:15.9	−43:03:53.78	344.838	−2.662	T	10.87	0.06
<b>CBF-3</b>	17:15:46.8	−42:24:06.12	345.434	−2.354	T	5.28	0.03
RPZM 8	17:15:51.6	−39:33:08.24	347.763	−0.711	T	9.35	0.09

the local ISM and therefore to the next generation of stars. Moreover, SNRs release large amounts of energy, generating shock waves that propagate in the immediate surroundings with evident effects (shaping of ISM, triggering star-formation, etc.).

The most complete catalogue of Galactic SNRs is provided by Green (2019) on the basis of observations performed over the whole electromagnetic spectrum. The large majority of the classified SNRs (~95 per cent) is identified as radio source.

In the ASKAP SCORPIO region there are 14 SNRs reported in Green (2019) and two candidates from the literature (Whiteoak & Green 1996), whose classification as SNRs has been recently supported by Ingallinera et al. (2019). All of them are visually detected in the SCORPIO map, and their main characteristics are summarized in Table 4. In the ASKAP map we also detect a further three SNR candidates, proposed by Ingallinera et al. (2019), namely SCO J165948–420527, SCO J170029–421309, and SCO J170105–420531.

SNRs are studied across the whole electromagnetic spectrum, but non-thermal radio emission remains their main identifier. The morphology and the spectral variations in the radio band are closely related to the evolutionary phase and the interaction of the SNR with the surrounding material. The possibility to observe these sources with high sensitivity and angular resolution in the radio band allows

us to identify new SNRs and to perform detailed morphological and spectral characterization of the known ones. Indeed, both the age and the environmental conditions can affect the emission processes in SNRs, and the study of a larger sample of objects is crucial to their wider understanding and classification.

Due to the availability of very short baselines, ASKAP allowed us to reach an LAS of ~50 arcmin at 912 MHz. This value, coupled with the high resolution, permits us to investigate SNRs at different angular scales, providing sensitive and detailed maps of these extended and complex sources. In the ASKAP map at 912 MHz, we can study the morphological details of the 16 known SNRs detected in the SCORPIO field. A  $2.3 \times 1.3$  deg<sup>2</sup> portion of the map, centred at  $l = 343.8^\circ$   $b = -0.2^\circ$ , is shown in Fig. 11, where four published SNRs (Green 2019) are highlighted with white circles and the three SNR candidates (Ingallinera et al. 2019) with green circles.

We stress here that the ASKAP mapping capabilities, illustrated in Fig. 4 for the SNR G343.1–0.7, allow us to distinguish the unrelated, field sources from the remnant itself. This results in a significant improvement in the estimation of the flux density of these SNRs with respect to previous images of these sources. Moreover, a previously classified SNR might be reclassified as S or C if observed with a better sensitivity and higher resolution.

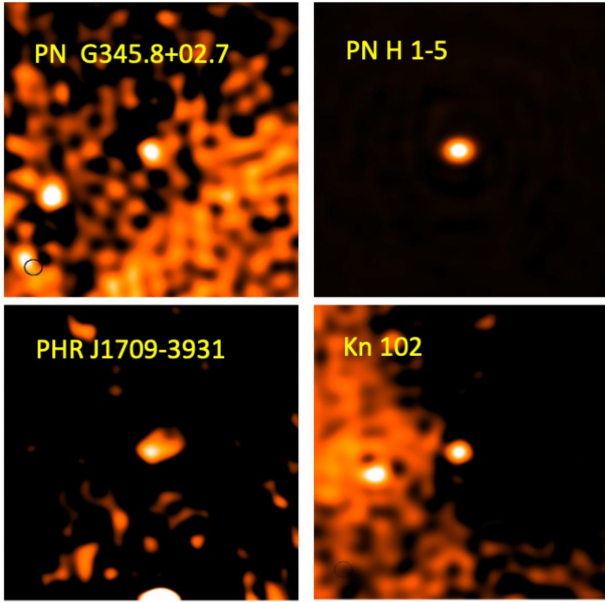


**Figure 9.** Maps of the detected PNe, including three new detections, which were not extracted by SELAVY, with no flux density indications in Table 3. All the images are 400 arcsec  $\times$  400 arcsec in size and centred at the PN's position (RA, Dec.).

In the radio, a large fraction of known SNRs present a typical ‘shell-like’ morphology, which is a strong indicator of their nature. There are many extended sources in the SCORPIO field that satisfy the morphological criterion for SNRs. Those sources constitute a very promising sample of SNR candidates. Observations at other frequencies, such as those already planned for the SCORPIO field between 0.9 and 1.8 GHz in the very near future, will be necessary to confirm the non-thermal origin of the radio emission.

## 4 THE SCORPIO PROJECT IN THE CONTEXT OF EMU: LESSONS LEARNT SO FAR

### 4.1 The impact of EMU on Galactic science

Radio surveys have provided a large number of unexpected discoveries, revealing different populations of radio-emitting objects and allowing numerous and very successful follow-up studies. An optimal radio survey of the Galactic plane needs to be carefully designed to correctly probe both the compact, extended and diffuse kinds of emission that populate the plane of the Galaxy. With previous and current radio facilities, this has been difficult to achieve in practice. The usual way to overcome this problem is the use of interferometric arrays in different antenna configurations and/or adding single-dish data. Up to now, existing interferometric radio continuum surveys of the Galactic plane cover a small portion of the Galactic plane (a few tens of square degrees), with high angular resolution (arcsecs) and sensitivity (1–2 mJy) (MAGPIS, Helfand et al. 2006; CORNISH, Hoare et al. 2012; THOR, Wang et al. 2018; GLOSTAR, Medina et al. 2019), or wider areas (several 100 square degrees) but with limited angular resolution (arcmins) and sensitivity (several mJy) (IGPS, Taylor et al. 2003, 2017; McClure-Griffiths et al. 2005; Stil et al. 2006).

There is therefore the necessity to have a well-designed survey of the Galactic plane, with a good compromise between sensitivity to extended diffuse emission and the ability to resolve more compact

sources. This is particularly important for the Southern hemisphere, where the lack of such surveys has prevented us from gathering detailed information of the radio properties of different source populations in the third and fourth Galactic quadrants. EMU, with its high sensitivity and angular resolution coupled to excellent short-spacing  $uv$ -plane coverage that provides high sensitivity to extended structures, and the unique survey speed capability that characterizes ASKAP, will allow us to create the most sensitive wide-field atlas of Galactic continuum emission yet made in the Southern hemisphere.

We stress that while the analysis presented here refers to data obtained with a partial deployment of ASKAP antennas, the tremendous potential of ASKAP has been clearly evidenced. ASKAP will be a revolutionary instrument for radio astronomy and therefore the full potential of EMU for Galactic observations can be anticipated. From this preliminary analysis of SCORPIO data, we have already demonstrated the unique capability of ASKAP to map complex sources, such as those that populate the Galactic plane, at different angular scales and with high sensitivity.

The EMU survey of the Galactic plane will have a profound impact on our understanding of star formation and stellar evolution, on Galactic structure and the nature of diffuse emission, and will very likely find new classes of objects.

### 4.2 The role of SCORPIO in the EMU design study

Several pilot studies, closely matching EMU in sensitivity and resolution, have been carried out to guide the design, operation, and science of the EMU project, e.g. the ATLAS (Norris et al. 2006) and SCORPIO (Paper I) surveys. SCORPIO, covering an area of a few square degrees, is the only pilot study to focus on low Galactic latitude and is especially important for the characterization of the Galactic sub-mJy population, providing a solid base-level from which we can better design some aspects of EMU. Indeed most of the ASKAP data processing techniques were optimized for extragalactic fields, and a special effort needs to be made to adapt processing techniques to cope with the large-scale structure, and strong confusing sources encountered in the Galactic plane. Synthesis imaging in these areas of the sky is badly affected by the discrete and limited sampling of the  $uv$ -plane. In the image plane this unavoidable imperfection arising from a lack of information in the  $uv$ -plane translates first into imaging artefacts, which increase the background noise in a non-random manner. It also likely results in incorrect reconstruction of the brightness distribution of extended sources. These problems are indeed detected in the ASKAP maps, where extended sources and the Galactic diffuse emission are present.

However, the comparison with the MGPS and the ATCA observations of SCORPIO reveals that the artefacts are not more severe than what we might theoretically expect. Indeed, the comparison of the same fields as observed by MOST, ASKAP, and ATCA demonstrates how ASKAP, even in this early-science phase, provides the best compromise between fine details and extended structures and shows a superior capability, compared to other radio facilities, to recover low-brightness diffuse emission up to angular scales comparable to its LAS, allowing us to efficiently probe different spatial scales in complex regions. This is particularly advantageous for Galactic studies.

A critical point in the ASKAP data reduction process is the gain calibration, performed as stated earlier by self-calibrating on bright sources automatically extracted from the observed field. The presence of diffuse emission and extended sources may result in poorly determined gain solutions. To overcome this limit, we constrained the self-calibration to regions of the  $uv$ -plane far from its

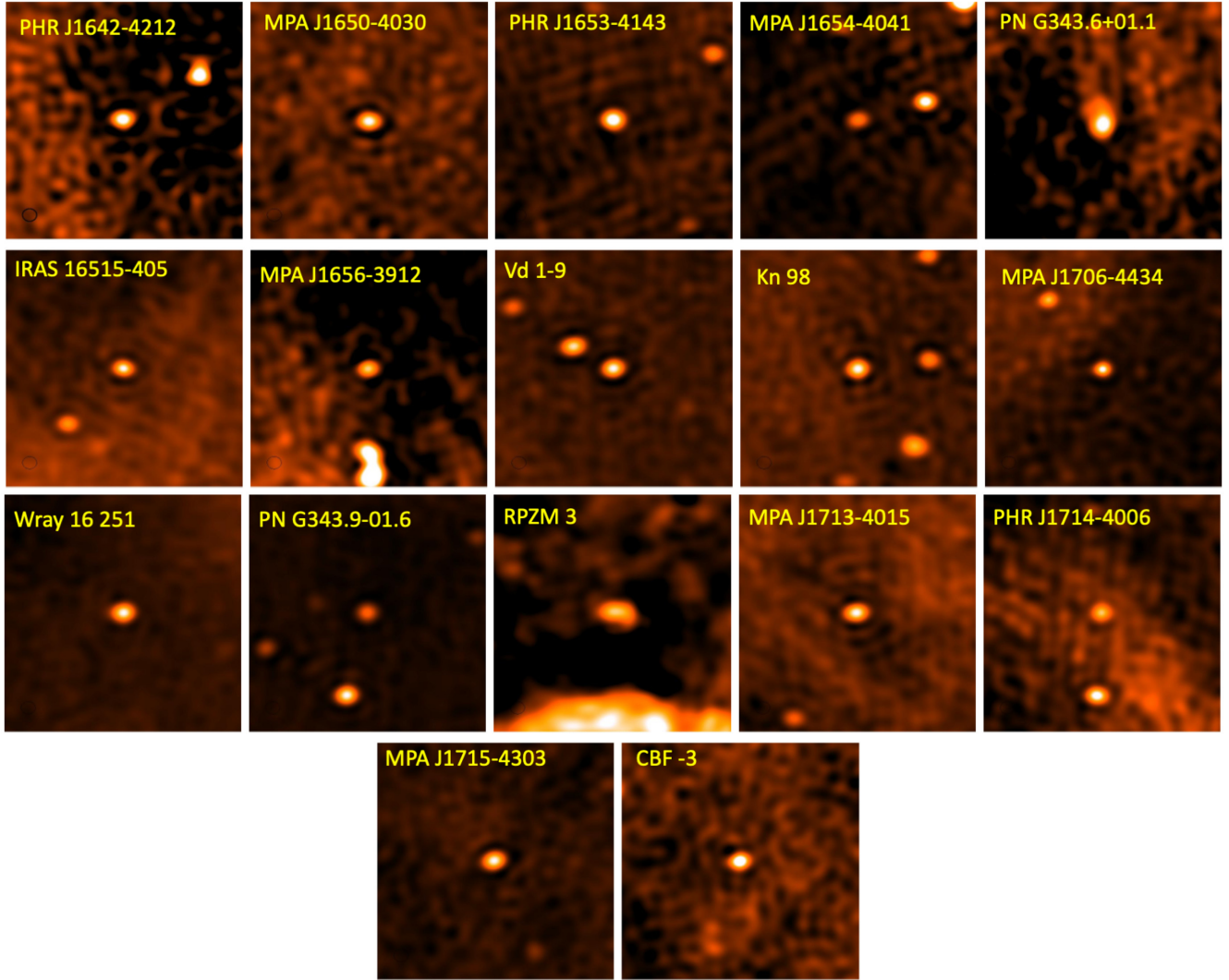


**Figure 10.** Maps of the new detected PNe, extracted by SELAVY (see Table 3). All the images are  $400 \text{ arcsec} \times 400 \text{ arcsec}$  in size and centred at the PN's position (RA, Dec.).

origin, i.e. restricting the analysis to long baselines (see Section 2.2). Several attempts were made in order to find an optimal setting that allowed us to filter out as much extended emission as possible but, at the same time, retain a sufficient number of baselines to derive reliable gain solutions. The ASKAP standard data reduction pipeline needs to be refined and adapted to this gain calibration process when applied to data acquired in the Galactic plane. A possible way to mitigate this problem is to design the EMU survey making sure to have a sequence of pointings, off the Galactic plane, alternating to pointings in the Galactic plane. This observing strategy would provide a sufficient number of point sources to be used for self-calibration.

The ASKAP observations were performed with three different pointings spaced by 51 arcmin, different from other fields observed with ASKAP in this early-science run. As reported in Section 2.2, two of these pointings, fields B and C, are corrupted by RFI. The automatic flagging algorithm embedded in the pipeline (CFLAG) failed to detect and flag these data. Another flagging utility (AOFLAGGER) was tested with similar results. Some single data sets have been visually inspected with CASA to check in detail whether the RFI

were confined to particular time intervals or frequency ranges. Therefore, before merging the three fields, a manual flag for bad data improved imaging of fields B and C. However, this approach is not straightforward because of the large amount of data (around 9 TB per each field) and will become totally impractical with the full ASKAP array, and when observing larger sky areas. We suggest that the ASKAP standard data reduction pipeline should improve the automated algorithm to mitigate and flag the RFI, taking also into account possible effects that the applied flagging methods could have on extended bright sources as those populating the Galactic plane (Bühr et al. 2016).

An important part of all the pilot studies in the pre-SKA era is to acquire the experience in handling data from SKA precursors that are representative of SKA. A significant challenge with these huge data sets, beyond the data reduction itself, is to automatically find and classify radio sources. The size of SCORPIO field is still small enough to allow source identification by visual inspection, as done in this paper, but it is also sufficiently large for testing and training automated algorithms. Results from the human-driven visual inspection can be used as a verification check of the automated

**Table 4.** Summary of the known SNR detected with ASKAP at 912 MHz in the SCORPIO field, and related main characteristics. Type of the SNR: ‘S’ or ‘C’ if the remnant shows a ‘shell’ or ‘composite’ radio structure. We report the frequency range within which each source has already been observed. Source sizes are reported according to Green (2019).

Source name	Type	Frequency range (GHz)	Source size (arcmin <sup>2</sup> )
G340.4–0.4*	S	0.330–5	10 × 7
G340.6+0.3	S	0.330–5	6 × 6
G341.2+0.9	C	0.330–1.425	22 × 16
G341.9–0.3	S	0.408–5	7 × 7
G342.0–0.2	S	0.408–5	12 × 9
G342.1+0.9	S	0.843–1.384	22 × 16
G343.1–0.7	S	0.843–8.55	27 × 21
G343.1–2.3	C?	0.330–8.46	32 × 32
G344.7–0.1	C?	0.408–11.2	8 × 8
G345.1–0.2	S?	0.843–1.4	6 × 6
G345.1+0.2	S	0.843	10 × 10
G345.7–0.2	S	0.843–5	6 × 6
G346.6–0.2	S	0.408–5	8 × 8
G347.3–0.5	S?	1.36	65 × 55
G348.5+0.1	S	0.08–14.7	15 × 15
G348.5–0.0*	S?	0.333–5	10 × 10

Note. \*This SNR is only partially detected at the edge of our ASKAP map.

algorithms. The pilot survey of SCORPIO has been already used as a test-bed for automated tools to extract sources, such as the CAESAR algorithm (Riggi et al. 2016, 2019) that extracts and parametrizes sources from astronomical radio interferometric maps.

The task for identifying the most appropriate method of finding and extracting sources, embedded in the diffuse emission expected at low Galactic latitude, is still ongoing (Riggi et al. 2021). The performance of the most used source finding algorithms (SELAVY, CAESAR, and AEGEAN) has been tested and it is subject of an ongoing work (Riggi et al., in preparation). A major result is that the number of false detections, above a fixed detection threshold, is considerable regardless of the finder used. This is due to the overdeblending of real diffuse emission and extended sources in the Galactic plane and to the presence of artefacts, due to a non-perfect cleaning. Overall, this represents a severe issue for future, large-scale radio surveys covering the Galactic plane such as those planned with ASKAP.

It is clear that with the new generation of large-scale surveys, which will be produced by new instruments such as the SKA and its precursors, it will be necessary to develop new automated algorithms able not only to extract both extended and compact sources but also to classify them. In the context of Galactic studies, exploiting the possibility of comparing different morphologies or different properties that sources manifest at different wavelengths, in automated methods and using data mining capabilities, could be particularly useful.

### 4.3 Synergies with existing Galactic plane surveys

Our view of the plane of the Galaxy has been completely revolutionized by a new generation of Galactic plane surveys as summarized by Hoare et al. (2012). Of particular interest are the surveys conducted at infrared and longer wavelengths, which can penetrate the extinction in the Galactic plane, tracing stars and nebulae (VVV; Minniti et al. 2010; GLIMPSE, Churchwell et al. 2006), the cold (HiGAL; Molinari et al. 2010), the warm (MIPSGAL, Carey et al. 2009; WISE, Wright, Eisenhardt & Mainzer 2010), and hot dust (GLIMPSE).

These new IR Galactic plane surveys are characterized by a few arcsecs angular resolution, matching the ASKAP angular resolution, and have a very good sensitivity and sky coverage, to allow IR and radio counterparts to be efficiently identified and studied. Studies of this kind will be facilitated by visual analytics tools that have been recently developed to assist scientists in managing, visualizing, and analysing large amount of data (Vitello et al. 2018).

While Galactic H II regions and PNe populations can be in principle discriminated by using IR colours derived by photometric measurements (Anderson et al. 2012) or studying their local environment (Irabor et al. 2018), in the case of H II regions and PNe, as well as for other classes of Galactic objects, robust classification can be achieved only by combining radio and IR information (Cohen et al. 2011).

The SCORPIO field, as observed by the ASKAP (see Fig. 2), reveals the striking ‘bubbling’ appearance of the Galactic plane, confirming what recent large-scale mid-IR surveys have revealed: the presence of hundreds of extended (scales from tens arcsec to arcminutes) gaseous and dusty nebulae ubiquitous in the Galactic plane. The term ‘bubbles’ is usually used to classify them, although they can be the result of different astrophysical phenomena: a bubble can be the result of the expansion of a young H II region into the ISM due to strong winds or radiation pressure from the central stellar object/s (Churchwell et al. 2006) or indicate the presence of circumstellar material, the signpost of instabilities that often characterize the late stages of stellar evolution (Gvaramadze, Kniazev & Fabrika 2010; Mizuno et al. 2010; Watcher et al. 2010). Such circumstellar envelopes (CSE) are often observed in PNe, LBVs, WRs, and SNRs. Several authors have pointed out that with enough resolution and sensitivity it is possible to classify Galactic bubbles, discriminating H II regions from evolved star CSEs, and among the latter low- and high-mass stars, just from the comparison of the observed morphology in the IR and in the radio (Watson et al. 2008; Deharveng et al. 2010; Ingallinera et al. 2016). Indeed, for H II regions or evolved stars, while the radio emission traces the ionized part of the circumstellar material, the emission observed in the IR traces emission from polycyclic aromatic hydrocarbons (PAH) and hot dust ( $\sim 8 \mu\text{m}$ ) or warm dust ( $\sim 24 \mu\text{m}$ ) or cool dust ( $\sim 70 \mu\text{m}$ ). In H II regions, the  $\sim 8 \mu\text{m}$  emission is dominated by PAH, which cannot survive at the temperature of the inner region, where the radio emission originates. Therefore, a strong ( $\sim 8 \mu\text{m}$ ) emission ‘wrapping around’ the radio emission points towards an H II region classification (Deharveng et al. 2010; Ingallinera et al. 2019).

In the case of SNRs, there is evidence of dust signatures in several of them (Chawner et al. 2020). However, the ratio of mid-IR to radio continuum emission results to be much lower than the infrared to radio ratio observed in H II regions (Pinheiro Goncalves et al. 2011). This can be used as efficient diagnostics to discriminate between a thermal and a non-thermal emitting bubble. A similar anticorrelation between radio emission and  $8 \mu\text{m}$  IR emission is also established (Brogan et al. 2006; Anderson et al. 2017).

There are many extended sources in the ASKAP SCORPIO field with a roundish or shell-like structure (bubbles) that satisfy the morphological criterion for SNRs but also for H II regions and evolved stars. Fig. 12 is a composite image of a portion of the ASKAP SCORPIO field, for  $341^\circ \leq l \leq 348^\circ$  and  $|b| \leq 1^\circ$  in both dust and ionized gas. Dust, as traced at 8 and  $70 \mu\text{m}$ , and ionized gas, probed by the radio, are cospatial at large scales in star-forming regions associated with H II regions, while there is a clear lack of dust associated with the radio in the case of known SNRs. The extended sources detected in SCORPIO therefore constitute a very promising

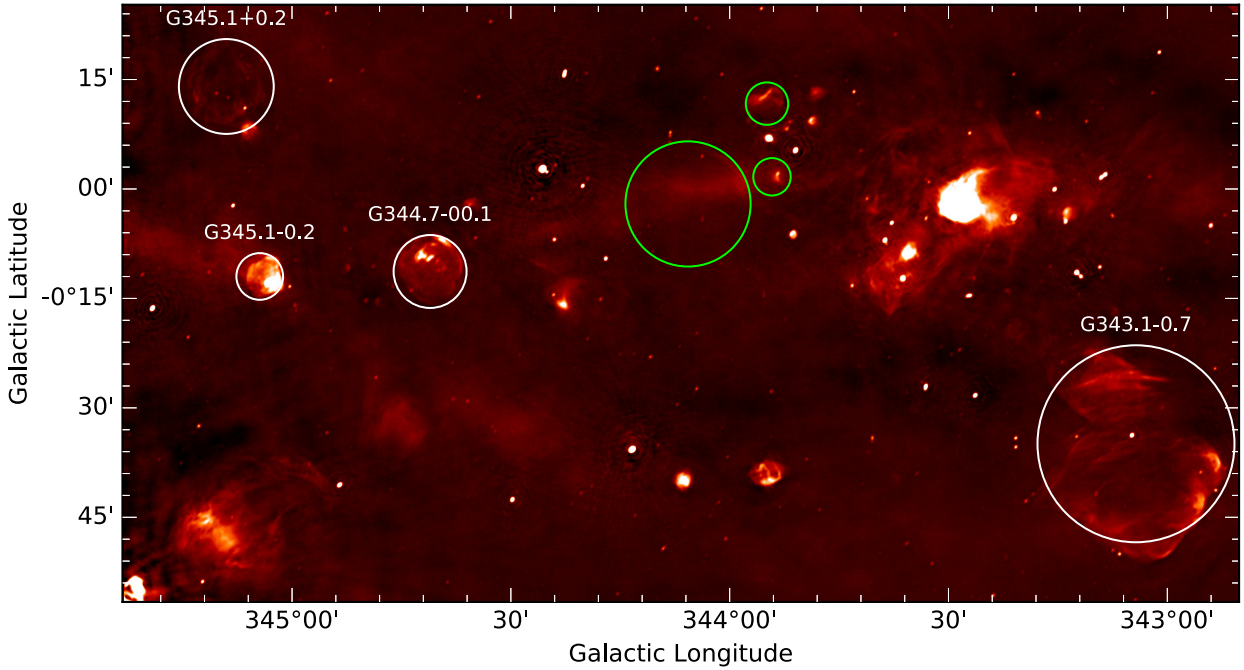


**Figure 11.** A zoom-in of the SCORPIO field, a  $2.3 \times 1.3 \text{ deg}^2$  portion of the map, centred at  $l, b = 343.8^\circ, -0.2^\circ$ . Known SNR (Green 2019) are highlighted with white circles, while proposed SNR candidates (Ingallinera et al. 2019) with green circles (see text for more details).

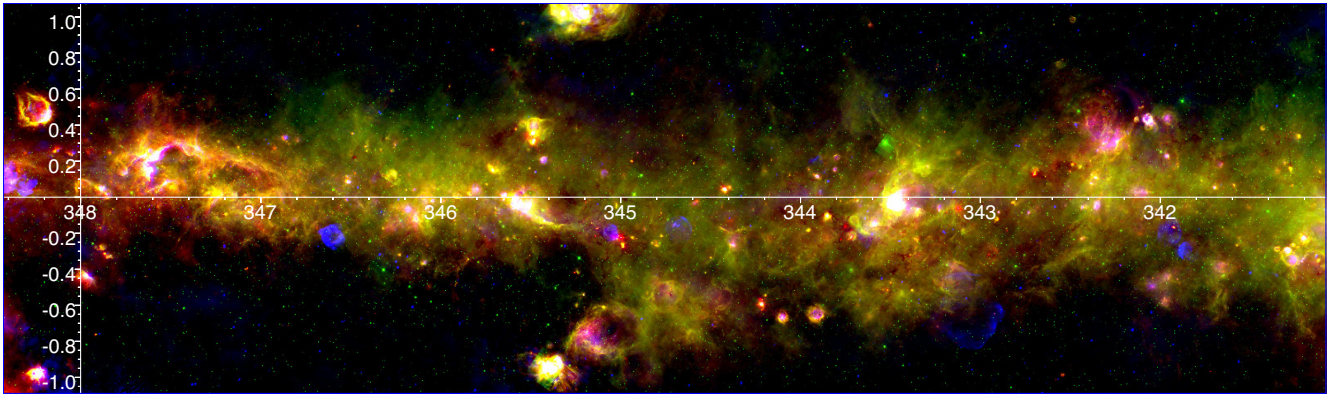


**Figure 12.** A composite image of a portion of the SCORPIO field ( $341^\circ \leq l \leq 348^\circ$ ). The colour-code is: green, from Spitzer/Glimpse (IRAC,  $8 \mu\text{m}$ ); red, from Herschel/Hi-GAL (PACS,  $70 \mu\text{m}$ ) and blue from ASKAP, 912 MHz. The 8 and  $70 \mu\text{m}$  emissions are tracers of the dust, while the radio emission traces of the ionized gas. Both dust and ionized emission are largely spatially coincident in star-forming regions, while there is very little correlation in the case of SNRs, which stand out due to their radio emission.

sample to classify the Galactic Bubbles and in particular to select new SNR candidates, by applying the criterion that bubbles with different origin are characterized by different IR emission, in both intensity and morphology. Different samples of ‘bubbles’ are in the process of being selected using these criteria. Further confirmation of their classification will be assessed on the basis of their radio spectra as determined by forthcoming planned ASKAP observations of the SCORPIO field at 0.9 and 1.8 GHz.

## 5 SUMMARY AND OUTLOOK

We present the ASKAP observations of the SCORPIO field, conducted in the ASKAP early-science framework. The ASKAP SCOR-

PIO field was observed in band 1 (central frequency 912 MHz) with three different pointings, for a total area of  $\sim 40$  square degrees. The data were processed using the ASKAPSOFT data reduction pipeline (version 0.19). Some fine-tuning was needed with respect to the standard settings of the pipeline in order to better deal with data acquired towards the Galactic plane. In particular, the self-calibration process was limited only to regions of the  $uv$ -plane with  $\sqrt{u^2 + v^2} > 1100 \text{ m}$ . The final map presents a median rms of  $541 \mu\text{Jy beam}^{-1}$ , but as low as  $130 \mu\text{Jy beam}^{-1}$  in regions far from the Galactic plane.

A total of 3545 sources were extracted from the image, only 75 percent of them are compatible with a point source. The presence

of a significant number of extended sources can be accounted for by Galactic sources, mainly H II regions. The comparison with the same areas of the Galactic plane as observed with the MGPS survey demonstrates the unique ASKAP capability of mapping complex sources, at different angular scales, with a trade-off between sensitivity to extended and diffuse emission and ability to reveal the finest details. This is the result of the ASKAP design to image wide fields with particular attention to the *uv*-coverage from short-baselines.

The SCORPIO project has been designed to forecast the scientific impact of the SKA and its precursors, such as ASKAP, on our view of the Milky Way. At the same time, SCORPIO has been considered as a test-bed to identify, and possibly overcome, technical issues arising from the complex structure of the Galactic plane. It is clear that SCORPIO has accomplished both its scientific and technical tasks. In particular, a good estimation of the potential of deep radio surveys for Galactic studies has been established.

Even with the presented results, obtained with ASKAP not fully deployed, the detection fraction of different Galactic populations emitting in the radio band has been significantly improved. We were able to detect all the known radio-emitting H II regions contained in the ASKAP SCORPIO field, and also a significant portion of H II regions previously classified as ‘radio quiet’. We have doubled the number of radio detections for PNe within the ASKAP SCORPIO field and obtained a detailed morphology of known and candidate SNRs. Our results have been achieved by visual inspection at positions from relevant, mostly optical, catalogues. When complete radio multifrequency and polarization information, obtained with the full array, is available, as planned in the near future for SCORPIO and more in general with EMU, it will be possible to identify different Galactic source populations, disentangling thermal and non-thermal emitters or pick-up stellar radio sources just from their polarization characteristics (Dulk & Marsh 1982). With regards to SNRs, SCORPIO ASKAP observations have already highlighted the effectiveness in searching for new candidates.

We plan to focus our future activities on discovering and characterizing different populations of Galactic sources and to work at least on the following topics: (a) complete catalogue of extended sources, including H II regions, SNRs, and more evolved PNe; (b) Characterization of known SNRs and classification of SNR candidates via multiband radio observations in synergy with mid-IR observations; and (c) Multiwavelength study of the SCORPIO field in synergy with mid-IR observations aimed at identifying new H II region, SNR, LBV, WR, and PN candidates and revealing the complete picture of complex regions within the field (i.e. giant molecular clouds).

## ACKNOWLEDGEMENTS

The Australian SKA Pathfinder is part of the Australia Telescope National Facility which is managed by CSIRO. Operation of ASKAP is funded by the Australian Government with support from the National Collaborative Research Infrastructure Strategy. Establishment of the Murchison Radio-astronomy Observatory was funded by the Australian Government and the Government of Western Australia. This work was supported by resources provided by the Pawsey Supercomputing Centre with funding from the Australian Government and the Government of Western Australia. We acknowledge the Wajarri Yamatji people as the traditional owners of the Observatory site. HA has benefitted from grant CIIC 90/2020 of Universidad de Guanajuato, Mexico. MJM acknowledges the support of the National Science Centre, Poland through the SONATA

BIS grant 2018/30/E/ST9/00208. C. B. benefited from grant No. 863448 (NEANIAS) of the Horizon 2020 European Commission programme. This research has made use of the HASH PN database at hashpn.space.

## DATA AVAILABILITY

The data underlying this article will be shared on reasonable request to the corresponding author.

## REFERENCES

- Anderson L. D., Bania T. M., Blaser D. S., Cunningham V., Wenger T. V., Johnstone B. M., Armentrout W. P., 2014, *ApJS*, 212, 1
- Anderson L. D., Zavagno A., Barlow M. J., García-Lario P., Noriega-Crespo A., 2012, *A&A*, 537, 1A.
- Anderson L. D. et al., 2017, *A&A*, 605, A58
- Armentrout W. P., Anderson L. D., Wenger T. V., Balser D. S., Bania T. M., 2021, *ApJS*, 253, 23A
- Becker R. H., White R. L., Helfand D. J., 1995, *ApJ*, 450, 559
- Bihr S. et al., 2016, *A&A*, 586, A97
- Brogan C. L., Gelfand J. D., Gaensler B. M., Kassim N. E., Lazio T. J. W., 2006, *ApJ*, 639, L25
- Carey S. J. et al., 2009, *PASP*, 121, 76
- Cavallaro F. et al., 2018, *MNRAS*, 473, 1685
- Chawner H. et al., 2020, *MNRAS*, 493, 2706
- Chippendale A. P., Hayman D., Hay S. G., 2014, *Publ. Astron. Soc. Aust.*, 31, 19
- Churchwell E. et al., 2006, *ApJ*, 649, 759
- Cohen M. et al., 2011, *MNRAS*, 413, 542
- Condon J. J., Kaplan D. L., 1998, *ApJS*, 117, 361
- Deharveng L. et al., 2010, *A&A*, 523, A6
- Dulk G. A., Marsh K. A., 1982, *ApJ*, 259, 350
- Eggen E. et al., 2017, *MNRAS*, 470, 2
- Green D. A., 2019, *JA&A*, 40, 36
- Gvaramadze V. V., Kniazev A. Y., Fabrika S., 2010, *MNRAS*, 405, 1047
- Helfand D. J., Becker R. H., White R. L., Fallon A., Tuttle S., 2006, *AJ*, 131, 2525
- Hoare M. et al., 2012, *PASP*, 124, 939
- Hotan A. W. et al., 2021, *Publ. Astron. Soc. Aust.*, 38, 9
- Ingallinera A. et al., 2016, *MNRAS*, 463, 723
- Ingallinera A. et al., 2019, *MNRAS*, 490, 5063
- Irabor T. et al., 2018, *MNRAS*, 480, 2423
- Jacoby G. H. et al., 2010, *Publ. Astron. Soc. Aust.*, 27, 156
- Kwok S., 2007, *The Origin, Evolution of Planetary Nebulae*. Cambridge University Press, Cambridge, UK
- Leahy D. A. et al., 2019, *Publ. Astron. Soc. Aust.*, 36, 24L
- McClure-Griffiths N. M. et al., 2005, *ApJS*, 158, 178
- McConnell D. et al., 2016, *Publ. Astron. Soc. Aust.*, 33, e042
- Medina S.-N. X. et al., 2019, *A&A*, 627, 175
- Minniti D. et al., 2010, *New Astron.*, 15, 433
- Mizuno D. R. et al., 2010, *AJ*, 139, 1542
- Molinari S. et al., 2010, *A&A*, 518, L100
- Murphy T., Mauch T., Green A., Hunstead R. W., Pietrzynska B., Kels A. P., Sztajer P., 2007, *MNRAS*, 382, 382
- Norris R. P. et al., 2006, *AJ*, 132, 2409
- Norris R. P. et al., 2011, *Publ. Astron. Soc. Aust.*, 28, 215
- Parker Q. A., Bojić I. S., Frew D. J., 2016, *J. Phys. Conf. Ser.*, 728, 032008
- Pinheiro Goncalves D. et al., 2011, *AJ*, 142, 47
- Riggi S. et al., 2016, *MNRAS*, 460, 1486
- Riggi S. et al., 2019, *Publ. Astron. Soc. Aust.*, 36, 37
- Riggi S. et al., 2021, *MNRAS*, 502, 60
- Sabin L. et al., 2014, *MNRAS*, 443, 3388
- Stil J. M. et al., 2006, *AJ*, 132, 1158
- Tammann G. A., Loeffler W., Schroeder A., 1994, *ApJS*, 92, 487.
- Taylor A. R., et al., 2003, *AJ*, 125, 3145
- Taylor A. R. et al., 2017, *AJ*, 153, 113

- Umana G. et al., 2015, *MNRAS*, 454, 902  
 Vitello et al., 2018, *Publ. Astron. Soc. Aust.*, 130, 084503  
 Wang Y. et al., 2018, *A&A*, 619, A124  
 Watcher S. et al., 2010, *AJ*, 139, 2330  
 Watson C. et al., 2008, *ApJ*, 681, 1341  
 Whiteoak J. B. Z., Green A. J., 1996, *A&AS*, 118, 329  
 Whiting M. software ASKAP Science Data Processor, et al., software ASKAP Science Data Processor 2019, Available at: <https://bitbucket.csiro.au/scm/casssoft/askapsoft.git>  
 Whiting M., Humphrey B., 2012, *Publ. Astron. Soc. Aust.*, 29, 371  
 Wright E. L., Eisenhardt P. R. M., Mainzer A. K., 2010, *AJ*, 140, 1868

## SUPPORTING INFORMATION

Supplementary data are available at *MNRAS* online.

**Table S1.** H II regions and H II regions candidates detected and extracted with SELAVY. This truncated table is intended to show

its content. The complete table is available in the online version of the journal.

Please note: Oxford University Press is not responsible for the content or functionality of any supporting materials supplied by the authors. Any queries (other than missing material) should be directed to the corresponding author for the article.

This paper has been typeset from a  $\text{\TeX}/\text{\LaTeX}$  file prepared by the author.